Article

Electrochemical Corrosion Behavior of CrFeCoNi and CrMnFeCoNi Coatings in Salt Solution

Caimei Wang [1], Yang Yu [2], Peng He [3], Jianjun Zhang [1], Xiaoyu Ma [4], Hua Zhang [1,*], Huizhao Li [1] and Minghao Shao [1]

[1] School of Mechanical Engineering, Beijing Institute of Petrochemical Technology, Beijing 102617, China
[2] State Key Laboratory of Hydraulic Engineering Simulation and Safety, Tianjin University, Tianjin 300350, China
[3] State Key Laboratory of Advanced Welding and Joining, Harbin Institute of Technology, Harbin 150001, China
[4] Capital Aerospace Mechinery Carporation Limited, Beijing 100076, China
[*] Correspondence: huazhang@bipt.edu.cn; Tel.: +86-135-2188-0280

Abstract: CrFeCoNi and CrMnFeCoNi coatings were prepared by laser remelting method. The grain boundary characteristics distribution of both coatings was investigated by electron backscattered diffraction technique. The results showed that the CrFeCoNi coating exhibited higher fraction of low angle grain boundaries and Σ3 boundaries compared to the CrMnFeCoNi coating. The corrosion properties of the CrFeCoNi and CrMnFeCoNi coatings in 3.5 wt% NaCl solution were identified by electrochemical method and localized electrochemical impedance spectroscopy technique. The results indicated that the CrFeCoNi coating had a higher corrosion resistance than the CrMnFeCoNi coating. The better corrosion resistance of the CrFeCoNi coating could be attributed to the high fraction of Σ3 boundaries and low fraction of the high angle boundaries.

Keywords: high entropy alloys coating; grain boundary characteristic; local impedance modulus; corrosion behavior

1. Introduction

High entropy alloys (HEA) have drawn considerable attention due to their prospect of industrial applications and excellent properties such as exceptional mechanical properties, good oxidation resistance, excellent thermal stability and high corrosion resistance [1–3]. Currently, HEA is usually produced by arc melting or additive manufacturing [4,5]. The HEA materials have high cost because they generally contain a large portion of expensive elements. Therefore, much attention has been focused on exploiting HEA coatings to reduce the cost and enlarge the application range. So far, various methods have been used to fabricate HEA coating, such as air plasma spraying, magnetron sputtering, arc cladding, cold spraying and laser cladding [6–11].

At present, considerable researches have been done to explore the corrosion properties of the HEA coatings. These studies are mainly concerned with the effect of different additives on the corrosion properties of HEA coating. These additives contain metal elements, rare oxide and graphene oxide. Fan et al. investigated the effect of Fe content on the corrosion behavior of AlCoCrFeNi HEA coatings [12]. They found that increasing Fe content contributed to improving the corrosion property of coatings. Cui et al. studied the effect of CeO_2 on corrosion behavior of FeCoNiCrMo HEA coating [13]. Ahmed et al. investigated the microstructure and corrosion properties of the MnCrFeCoNi high entropy alloy-graphene oxide composite coatings [14]. The results showed that the corrosion resistance of coatings increased with the addition of graphene oxide. Additionally, some researchers have explored the effect of grain refinement on corrosion behavior of HEA coatings. Zhang et al. investigated the corrosion property of the $Al_{1.5}CoCeFeMnNi$ HEA coating after ultrasonic impact treatment [15]. They found that the grain was refined

and the corrosion resistance was improved. Fan et al. studied the corrosion property of ultrasonic induced AlCoCrFeNi HEA coating [16]. The results indicated that ultrasonic treatment contributed to increasing the segregation of Cr in grain boundaries, thereby improving the corrosion resistance.

Reports about the effect of grain boundary characteristics on corrosion behavior of HEA coatings are limited. It is well known that grain boundary characteristic distributions have an important effect on the corrosion behavior of polycrystalline alloys. Many previous reports have indicated that a large fraction of special grain boundaries (low CSL boundary) would improve the corrosion resistance of alloys [17,18]. An et al. [19] have reported that the corrosion rate of the CoNiFe alloys decreased when increasing the fraction of low special coincidence site lattice (CSL) boundaries. It has been reported that increasing low CSL grain boundaries ($\leq\Sigma29$) could provide better corrosion resistance to the steel [20,21]. The modification of the grain boundary character is generally achieved by annealing or inclusion of other elements. There is limited literature covering the information about the effect of additive elements on grain boundary character of HEA coating. The corrosion behavior of HEA coatings was generally studied by the traditional electrochemical method. This method could not distinguish the difference of the corrosion resistance between the grain boundary and grain interior as it measures the average current values for the whole surface of the electrode in contact with the solution. It is necessary to apply auxiliary techniques to probe the surface characteristics of HEA coatings in microscale. Localized electrochemical impedance spectroscopy (LEIS) was an effective tool for exploration of the electrode heterogeneity [22,23]. The objective of this study is to combine the grain boundary character with LEIS characterization to reveal the corrosion properties of HEA coatings.

In this study, CrFeCoNi and CrMnFeCoNi coatings were prepared by laser remelting method. The corrosion behavior of the CrFeCoNi and CrMnFeCoNi coatings in 3.5 wt% NaCl solution was analyzed by electrochemical method and LEIS measurements.

2. Materials and Methods

The commercial CrMnFeCoNi and CrFeCoNi powders with a size range between 15 and 53 μm were used as the feedstock. The CrMnFeCoNi and CrFeCoNi coatings were prepared on the X65 steel substrate by laser remelting method. The compositions of the substrate are shown in Table 1. The as-prepared coatings were characterized by electron backscattered diffraction (EBSD)technique to reveal the microstructure and phase composition. The chemical compositions of these coatings were investigated by energy dispersive spectroscopy (EDS, IE 350).

Table 1. Chemical composition of X65 steel substrate.

Material	Fe	Cr	Mn	Ni	C	P	Cu	Si	Nb	V	Ti	Mo
Substrate (wt.%)	Bal	0.25	1.60	0.30	0.09	0.02	0.30	0.35	0.06	0.06	0.02	0.30

Electrochemical workstation (PGSTAT302N) was used to evaluate the corrosion performance of coatings. The samples were cut into 3 mm × 3 mm for electrochemical tests. The tests were carried out using a traditional three electrodes system including a platinum sheet counter electrode, a saturated calomel reference electrode (SCE) and a working electrode (coating sample with an exposed area of 0.09 cm^2). The open circuit potential (OCP) of the CrMnFeCoNi and CrFeCoNi coatings was investigated for 2 h to reveal the passive behavior. Cyclic polarization curves of the CrMnFeCoNi and CrFeCoNi coatings were measured at a scan rate of 0.0005 V/s. The reverse scanning was carried out when the anode current density was higher than 1 mA/cm^2. The potentiostatic tests were conducted at applied potential of -0.1 V$_{SCE}$. The electrochemical impedance spectroscopy (EIS) was investigated under the condition of OCP by applying a 10 mV amplitude signal in the frequency range from 100 kHz to 0.01 Hz. All the above tests were performed in 3.5 wt%

NaCl solution at room temperature and repeated at least three times. Scanning Kelvin probe tests were carried out using the micro-scanning electrochemical workstation (VersaS-CAN, Ametek Scientific Instrucments, USA). LEIS measurements were conducted for the CrFeCoNi and CrMnFeCoNi coatings using a VersaSCAN Scanning Electrochemical Workstation. The LEIS maps of surface distribution of the impedance module were ascertained for the scanned area of 100×100 μm.

3. Results and Discussions

Figure 1 shows the cross sectional EBSD images of the CrFeCoNi and CrMnFeCoNi coatings. As shown in Figure 1a,b, it can be observed that the CrFeCoNi and CrMnFe-CoNi coatings were composed of columnar dendrites. Moreover, the growth direction of dendrites was perpendicular to the fusion line due to high temperature gradient. No macro-segregation and solidification cracking were found, indicating that laser remelting method could effectively avoid these defects. Figure 1c and d indicated that the CrFeCoNi and CrMnFeCoNi coatings exhibited face centered cubic (FCC) structures [24]. This suggested that no phase transformation occurred during laser cladding process. The chemical composition of these two coating was investigated by EDS, and the results were shown in Table 2. Compared to original coating powders, the CrFeCoNi and CrMnFeCoNi coatings possessed higher Fe content.
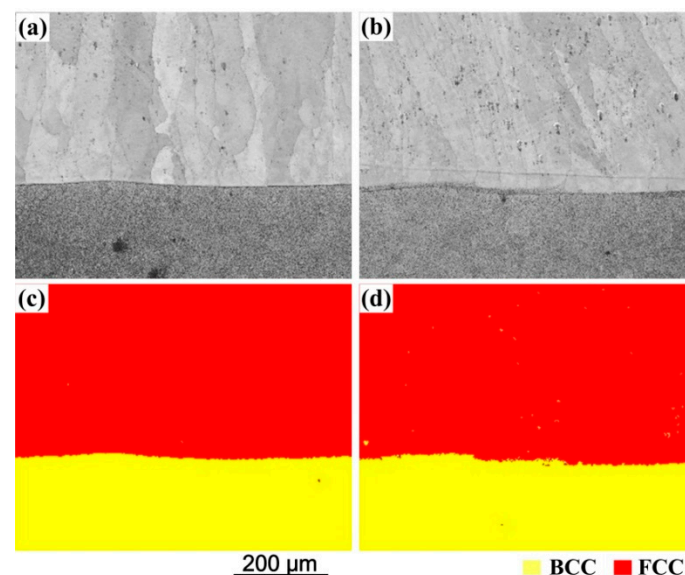

Figure 1. Cross sectional EBSD images of the CrFeCoNi and CrMnFeCoNi coatings: band contrast (**a**) and phase distribution (**c**) of CrFeCoNi coating; band contract (**b**) and phase distribution (**d**) of CrMnFeCoNi coating.

Table 2. Chemical compositions of CrFeCoNi and CrMnFeCoNi coatings.

Elements	Fe (at%)	Co (at%)	Ni (at%)	Cr (at%)	Mn (at%)
CrFeCoNi	29.00	24.25	24.00	22.75	-
CrMnFeCoNi	22.09	17.60	18.84	20.35	21.11

Figure 2 shows the misorientation angle distribution of the CrFeCoNi and CrMnFe-CoNi coatings. In both coatings, the misorientation in the range of 0° to 5° was observed, indicating the existence of low angle grain boundaries. The fraction of misorientation angle less than 5° of the CrFeCoNi and CrMnFeCoNi coating was 68.9% and 50.4%. This indicated that the CrFeCoNi coating had higher low angle grain boundaries (LAGBs) than the CrMnFeCoNi coating. The misorientation less than 10° was defined as low angle grain boundaries. By calculation, the fraction of LAGBs of the CrFeCoNi and CrMnFeCoNi

coatings were 68.9% and 50.8%. Figure 3 shows the fraction of low CSLs and Σ3 CSLs. The fraction of low CSLs exhibited higher in CrFeCoNi coating. The fraction of Σ3 CSLs was found to be more in the CrFeCoNi coating (3.5%) than in the CrMnFeCoNi coating (1.5%).
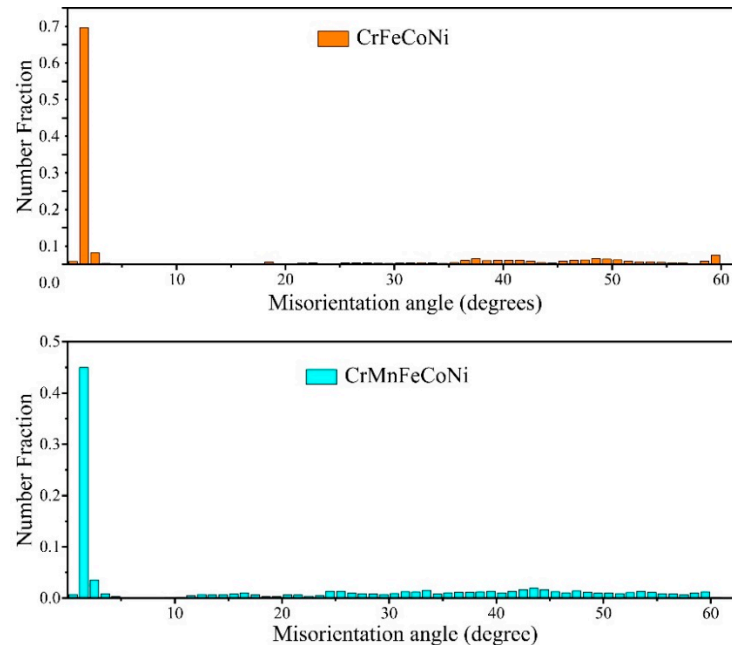

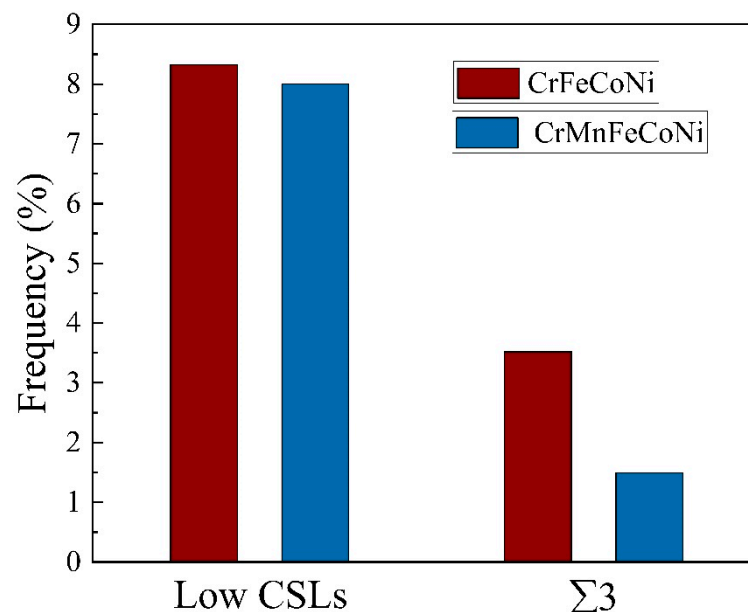**Figure 2.** Histogram representing misorientation angle distribution of the CrFeCoNi and CrMnFe-CoNi coatings.

Figure 3. Histogram representing the low CSLs fraction and Σ3 CSL fraction in the CrFeCoNi and CrMnFeCoNi coatings.

Figure 4 shows the open circuit potential of the CrFeCoNi and CrMnFeCoNi coatings in 3.5 wt% NaCl solution. At the initial stage, the OCP of the CrFeCoNi and CrMnFeCoNi coatings sharply increased with increasing immersion time. Subsequently, the OCP exhibited a relatively stable state. The increase of the OCP value was due to the formation of protective passive film. The OCP curve of the CrMnFeCoNi coating exhibited numerous spikes towards the negative direction. All the spikes showed a sharp decline followed by a

relatively slow rise. This situation was related to the generation, growth and repassivation of metastable pitting [25,26]. The largest potential spikes could reach 50 mV. No evident potential spike was found in the OCP curve of the CrFeCoNi coating, indicating the formation of stable passive film.
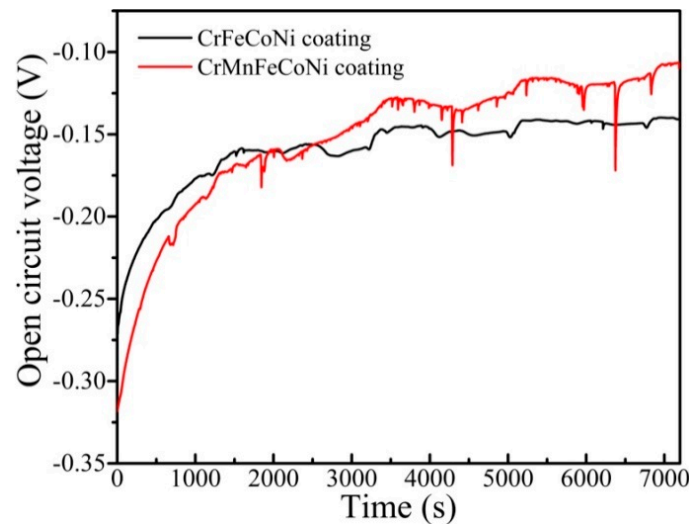

Figure 4. Open circuit potential of the CrFeCoNi and CrMnFeCoNi coatings in 3.5 wt% NaCl solution.

Figure 5 shows the cyclic potentiodynamic polarization curves of the CrFeCoNi and CrMnFeCoNi coatings in 3.5 wt% NaCl solution. It was found that both coatings exhibited immediate passivation, indicating the formation of passive film. The passive region of the CrFeCoNi coating was larger than that of the CrMnFeCoNi coating. The breaking potentials of the CrFeCoNi and CrMnFeCoNi coatings were 0.3 and 0.125 V, respectively. Numerous spikes were found in the passivation zone of the CrMnFeCoNi coating due to the metastable pitting. However, no spike could be observed in the passivation zone of the CrFeCoNi coating indicating that a stable passive film was formed. Both coatings showed hysteresis rings, and the annular area of the CrMnFeCoNi coating was obviously larger than that of the CrFeCoNi coating [27]. This indicated that the CrMnFeCoNi coating possessed higher pitting sensitivity.
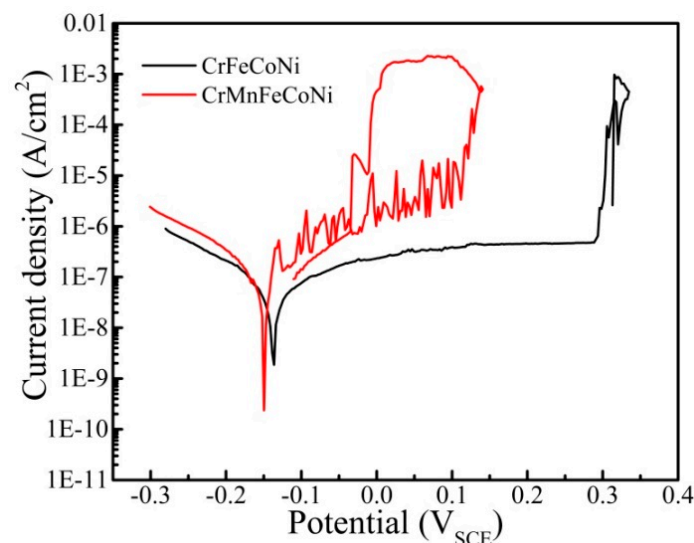

Figure 5. Cyclic potentiodynamic polarization curves of the CrFeCoNi and CrMnFeCoNi coatings in 3.5 wt% NaCl solution.

In order to investigate the passive behavior of both coatings in 3.5 wt% NaCl solution, potentiostatic polarization tests were carried out to analyze the current transient. Figure 6 shows the current-time transient curves of the CrFeCoNi and CrMnFeCoNi coatings at applied voltage of -0.1 V_{SCE} for 2 h in 3.5 wt% NaCl solution. It was found that the current density of both curves initially exhibited decreased sharply, and then presented a relatively stable state [28,29]. Figure 7 shows the local current-time transient curves of the CrFeCoNi and CrMnFeCoNi coatings at applied voltage of -0.1 V_{SCE} in 3.5 wt% NaCl solution. Numerous spikes were observed in the CrMnFeCoNi coating, while few spike could be found in the CrFeCoNi coating, which was consistent with the result of potentiodynamic polarization test. These spikes could be attributed to the formation of metastable pitting. The formation of stable pitting was directly related to the amount of metastable pitting. The CrMnFeCoNi coating exhibited a higher amount of metastable pitting, indicating that it had a higher pitting sensitivity. Additionally, the passive current density of the CrFeCoNi coating was lower than that of the CrMnFeCoNi coating, suggesting that the CrFeCoNi coating had better ability to resist corrosion attack.
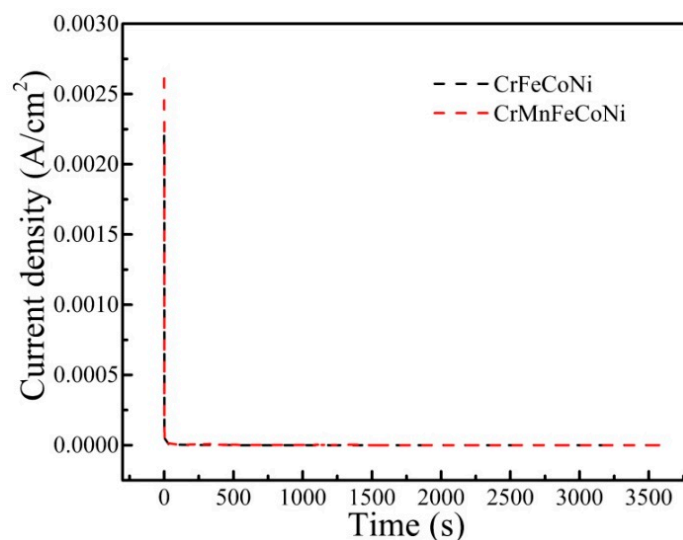

Figure 6. Current-time transient curves of the CrFeCoNi and CrMnFeCoNi coatings at applied voltage of -0.1 V_{SCE} for 2 h in 3.5 wt% NaCl solution.
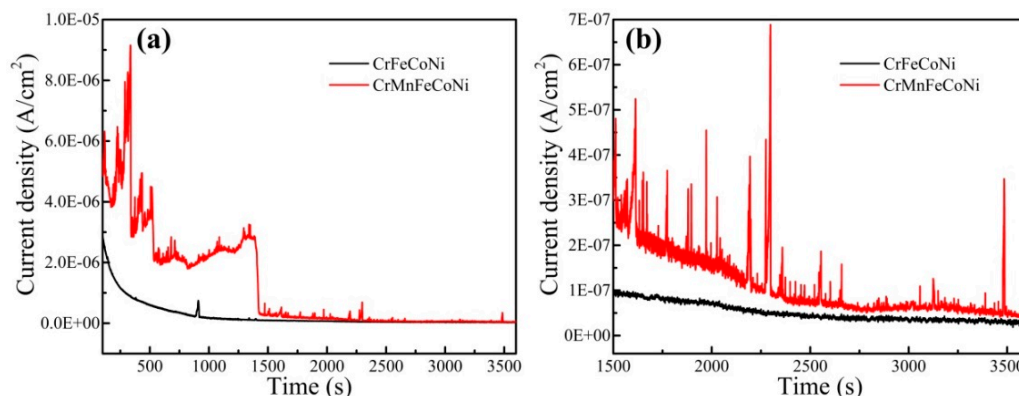

Figure 7. Current-time transient curves of the CrFeCoNi and CrMnFeCoNi coatings at applied voltage of -0.1 V_{SCE} in 3.5 wt% NaCl solution: (**a**) Current-time transient curve; (**b**) Local current-time transient curve.

Figure 8 shows the logi-logt plots for the CrFeCoNi and CrMnFeCoNi coatings at applied voltage of -0.1 V_{SCE} in 3.5 wt% NaCl solution. The relationship of current density and time could be used to determine the passive index, which could evaluate the property

of passive film [30]. By fitting, it can be certain that the passive index of the CrFeCoNi and CrMnFeCoNi coatings was 0.88 and 0.69, respectively. High passive index meant higher stability of passive film. The CrFeCoNi coating exhibited a higher passive index, suggesting it had higher corrosion resistance.
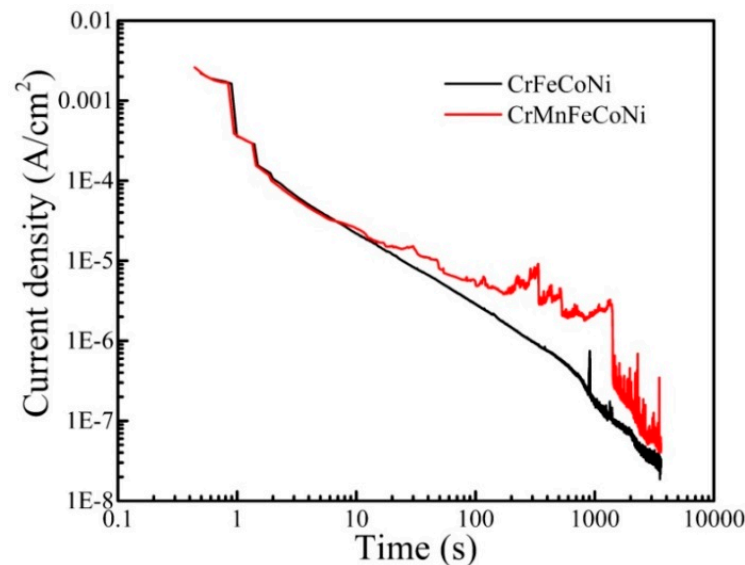

Figure 8. Logi-logt plots for the CrFeCoNi and CrMnFeCoNi coatings at applied voltage of 0.1 V$_{SCE}$ in 3.5 wt% NaCl solution.

Figure 9a shows the Nyquist diagrams of the CrFeCoNi and CrMnFeCoNi coating in 3.5 wt% NaCl solution at OCP condition. Both curves show unfinished semicircles, and the CrFeCoNi coating had a larger diameter of capacitive arc compared to the CrMnFeCoNi coating. A higher capacitive arc diameter indicates stronger corrosion resistance. Therefore, the CrFeCoNi coating had higher corrosion resistance. Figure 10b shows the Bode plots of the CrFeCoNi and CrMnFeCoNi coating in 3.5 wt% NaCl solution at OCP condition. At the high frequency region, the impedance modulus of the two coatings were close to constant, representing solution resistance. At the low frequency area, the CrFeCoNi coating exhibited larger impedance modulus compared to the CrMnFeCoNi coating, indicating larger polarization resistance. At intermediate frequency range, the slope of logZ-logf was close to −1 in both coatings. The maximum phase angle value of the two coatings were close to 90°.
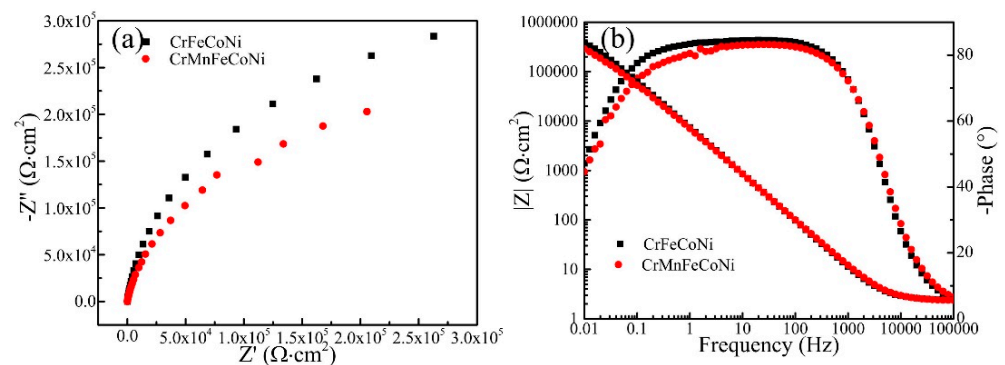

Figure 9. Nyquist diagrams (**a**) and Bode plots (**b**) of the CrFeCoNi and CrMnFeCoNi coating in 3.5 wt% NaCl solution at OCP condition.
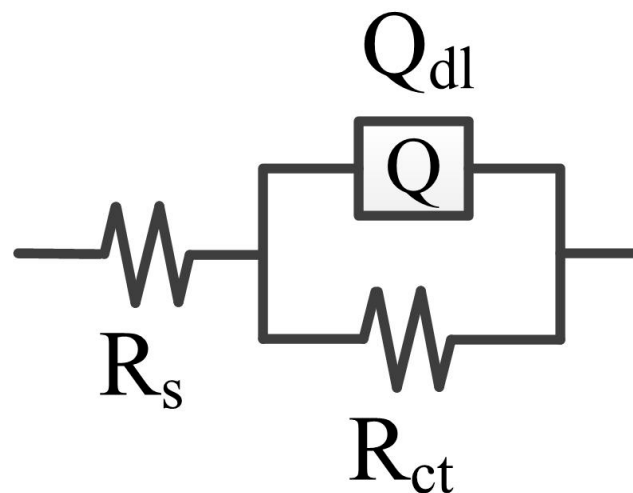
Figure 10. EEC for the analysis of the EIS of the CrFeCoNi and CrMnFeCoNi coatings at open circuit potential condition in 3.5 wt% NaCl solution.

Electrical equivalent circuit (EEC) was used to quantitatively analyze the corrosion resistance of coatings [31]. Figure 10 shows the EEC for the analysis of the EIS of the CrFeCoNi and CrMnFeCoNi coatings at open circuit potential condition in 3.5 wt% NaCl solution. Rs represents solution resistance, Rct signifies charge transfer resistance, and Qdl is the double layer capacitance. The fitting results are shown in Table 3. The fitting error value ($\Sigma c2$) was small, which indicated the good fitting quality. The charge transfer resistance of the CrFeCoNi ($5.91 \times 105 \ \Omega \cdot cm^2$) coating was larger than that of CrMnFeCoNi coating ($4.04 \times 105 \ \Omega \cdot cm^2$). This indicated that the passive film formed on the CrMnFeCoNi coating was more susceptible to corrosion attack. Therefore, the CrFeCoNi coating possessed better corrosion resistance.

Table 3. EEC fitting parameters for electrochemical impedance spectra in 3.5 wt% NaCl solution under OCP condition.

Heading	CrFeCoNi	CrMnFeCoNi
R_s (Ω cm^2)	2.43	2.36
R_{ct} (Ω cm^2)	5.91×10^5	4.04×10^5
Q_{dl} (Ω^{-1} cm^{-2} s^n)	2.42×10^{-5}	2.73×10^{-5}
n	0.94	0.92
Σc^2	3.43×10^{-4}	4.94×10^{-4}

Figure 11 shows the maps of the impedance module distribution on the surface of the CrFeCoNi and CrMnFeCoNi coatings in 3.5 wt% NaCl solution. The overall local impedance modulus value of the CrFeCoNi coating was higher than that of the CrMnFeCoNi coating, indicating the former had lower corrosion reaction activity. This result was consistent with the results of electrochemical tests. It is noticeable that the local impedance modulus values were slightly lower but of the same order of magnitude than those of bulk impedance values obtained by the EIS measurements due to internal stress causing microcracks in the electrode. A similar phenomenon was also found by another report [32]. In both coatings, the grain boundaries exhibited higher impedance modulus than the grain interiors. Therefore, in the process of corrosion, the grain boundaries would function as anode, while the grain interiors would function as cathode. It was observed that the anode and cathode evenly distributed along the grain boundaries.
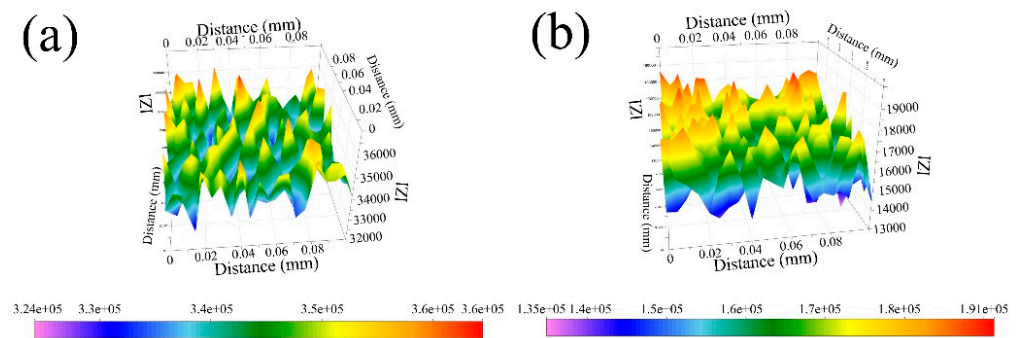
Figure 11. Maps of the impedance module distribution on the surface of the CrFeCoNi (**a**) and CrMnFeCoNi (**b**) coatings in 3.5 wt% NaCl solution.

The results of the potentiodynamic polarization, EIS and local impedance modulus indicate that the CrFeCoNi coating has superior corrosion resistance than the CrMnFeCoNi coating. The high corrosion resistance of the CrFeCoNi coating could be elaborated by the following reasons. On one hand, the CrFeCoNi coating exhibited higher fraction of LAGBs (Figure 2) and Σ3 boundaries (Figure 3) as well as lower high angle boundaries (Figure 3) compared to the CrMnFeCoNi coating. The Σ3 boundaries have low energy, which are inert to corrosion. The high angle boundaries would provide the corrosive media pathway to seep into the coating, which are the most favorable sites for pit formation. A similar phenomenon was found by other reports [33,34]. Thereby, the high fraction of Σ3 boundaries and low fraction of the high angle boundaries are responsible for the better corrosion resistance of the CrFeCoNi coating. Jin et al. also showed that the high fraction of Σ3 boundaries and low angle grain boundaries resulted in a better corrosion resistance of the Ni-W coating [35]. On the other hand, the CrFeCoNi coating exhibited higher local impedance modulus values compared to the CrMnFeCoNi coating. In both coatings, the impedance modulus value of the grain boundaries (anode) was higher than that of the grain interiors (cathode), which caused a galvanic effect. The high difference of the impedance modulus value of the anode and cathode would increase the driving force of corrosion. The difference of the impedance modulus values between the grain boundaries and grain interiors in the CrMnFeCoNi coating was larger than that of in the CrFeCoNi coating, thereby aggravating the decrease of the corrosion resistance of the CrMnFeCoNi coating and aggravating the pitting sensibility of the CrMnFeCoNi coating.

4. Conclusions

In this study, CrFeCoNi and CrMnFeCoNi coatings were fabricated by laser remelting method. Their grain boundary characteristics distribution and corrosion behavior were investigated. The main conclusions are as follows:

(1) The CrFeCoNi and CrMnFeCoNi coatings exhibited single phase structures. The CrFeCoNi coating had a higher fraction of LAGBs, low CSL boundaries and Σ3 boundaries than the CrMnFeCoNi coatings.

(2) The electrochemical tests results indicated that the CrFeCoNi coating exhibited lower corrosion current density, passive current density, pitting sensibility and higher charge transfer resistance than the CrMnFeCoNi coating, indicating that the CrFeCoNi coating possessed better corrosion resistance.

(3) The localized electrochemical impedance spectroscopy results showed the overall local impedance modulus value of the CrFeCoNi coating was higher than that of the CrMnFeCoNi coating, indicating the former had lower corrosion reaction activity.

(4) The better corrosion resistance of the CrFeCoNi coating could be attributed to the high fraction of Σ3 boundaries, low fraction of the high angle boundaries and high local impedance modulus value.

References

1. Yeh, J.W.; Chen, S.K.; Lin, S.J.; Gan, J.Y.; Chin, T.S.; Shun, T.T.; Tsau, C.H.; Chang, S.Y. Nanostructured high-entropy alloys with multiple principal elements: Novel alloy design concepts and outcomes. *Adv. Eng. Mater.* **2004**, *6*, 229–303. [CrossRef]
2. Cantor, B.; Chang, I.T.H.; Knight, P.; Vincent, A.J.B. Microstructural development in equiatomic multicomponent alloys. *Mater. Sci. Eng. A* **2004**, *375–377*, 213–218. [CrossRef]
3. Vaidya, M.; Trubel, S.; Murty, B.S.; Wilde, G.; Divinski, S.V. Ni trace diffusion in CoCrFeNi and CoCrFeMnNi high entropy alloys. *J. Alloy. Compd.* **2016**, *688*, 994–1001. [CrossRef]
4. Lin, D.Y.; Xu, L.Y.; Jing, H.Y.; Han, Y.D.; Zhao, L.; Minami, F. Effects of annealing on the structure and mechanical properties of FeCoCrNi high-entropy alloy fabricated via selective laser melting. *Addit. Manuf.* **2020**, *32*, 101058. [CrossRef]
5. Miracle, D.B.; Senkov, O.N. A critical review of high entropy alloys and related concepts. *Acta Mater.* **2017**, *122*, 448–511. [CrossRef]
6. Meghwal, A.; Anupam, A.; Luzin, V.; Schulz, C.; Hail, C.; Murty, B.S.; Kottada, R.S.; Berndt, C.C.; Ang, A.S.M. Multiscale mechanical performance and corrosion behaviour of plasma sprayed AlCoCrFeNi high-entropy alloy coatings. *J. Alloy. Compd.* **2021**, *854*, 157140. [CrossRef]
7. Wang, C.M.; Yu, J.X.; Zhang, Y.; Yu, Y. Phase evolution and solidification cracking sensibility in laser remelting treatment of the plasma-sprayed CrMnFeCoNi high entropy alloy coating. *Mate. Des.* **2019**, *182*, 108040. [CrossRef]
8. Wang, C.M.; Yu, Y.; Yu, J.X.; Zhang, Y.; Wang, F.C.; Li, H.D. Effect of the macro-segregation on corrosion behavior of CrMnFeCoNi coating prepared by arc cladding. *J. Alloy. Compd.* **2020**, *846*, 156263. [CrossRef]
9. Ye, Q.F.; Feng, K.; Li, Z.G.; Lu, F.G.; Li, R.F.; Huang, J.; Wu, Y.X. Microstructure and corrosion properties of CrMnFeCoNi high entropy alloy coating. *Appl. Surf. Sci.* **2017**, *396*, 1420–1426. [CrossRef]
10. Yin, S.; Li, W.Y.; Song, B.; Yan, X.C.; Kuang, M.; Xu, Y.X.; Wen, K.; Lupoi, R. Deposition of FeCoNiCrMn high entropy alloy (HEA) coating via cold spraying. *J. Mater. Sci. Technol.* **2019**, *35*, 1003–1007. [CrossRef]
11. Zhao, Y.M.; Zhang, X.M.; Quan, H.; Chen, Y.J.; Wang, S.; Zhang, S. Effect of Mo addition on structures and properties of FeCoNiCrMn high entropy alloy film by direct current magnetron sputtering. *J. Alloy. Compd.* **2022**, *895*, 162709. [CrossRef]
12. Fan, Q.K.; Chen, C.; Fan, C.L.; Liu, Z.; Cai, X.Y.; Lin, S.B. AlCoCrFeNi high-entropy alloy coatings prepared by gas tungsten arc cladding: Microstructure, mechanical and corrosion properties. *Intermetallics* **2021**, *138*, 107337. [CrossRef]
13. Cui, C.; Wu, M.P.; Miao, X.J.; Zhao, Z.S.; Gong, Y.L. Microstructure and corrosion behavior of CeO2/FeCoNiCrMo high-entropy alloy coating prepared by laser cladding. *J. Alloy. Compd.* **2022**, *890*, 161826. [CrossRef]
14. Aliyu, A.; Srivastava, C. Microstructure and corrosion properties of MnCrFeCoNi high entropy alloy-graphene oxide composite coatings. *Materialia* **2019**, *5*, 100249. [CrossRef]
15. Zhang, Q.; Li, M.Y.; Han, B.; Zhang, S.Y.; Li, Y.; Hu, C.Y. Investigation on microstructures and properties of Al1.5CoCrFeMnNi high entropy alloy coating before and after ultrasonic impact treatment. *J. Alloy. Compd.* **2021**, *884*, 160989. [CrossRef]
16. Fan, Q.K.; Chen, C.; Fan, C.L.; Liu, Z.; Cai, X.Y.; Lin, S.B.; Yang, C.L. Ultrasonic induces grain refinement in gas tungsten arc cladding AlCoCrFeNi high-entropy alloy coatings. *Mater. Sci. Eng. A* **2021**, *821*, 141607. [CrossRef]
17. Bechtle, S.; Kumar, M.; Somerday, B.P.; Launey, M.E.; Ritchie, R.O. Grain-boundary engineering markedly reduces susceptibility to intergranular hydrogen embrittlement in metallic materials. *Acta Mater.* **2009**, *57*, 4148–4157. [CrossRef]
18. Huang, Q.B.; Wang, Z.; Ding, H.; Xi, J.; Fu, W. Dependence of corrosion resistance on grain boundary characteristics in a high nitrogen CrMn austenitic stainless steel. *J. Mater. Sci. Technol.* **2017**, *33*, 1621–1628.
19. An, X.L.; Chu, C.L.; Zhou, L.; Ji, J.; Shen, B.L.; Chu, P.K. Controlling the corrosion behavior of CoNiFe medium entropy alloy by grain boundary engineering. *Mater. Charact.* **2020**, *164*, 110323. [CrossRef]
20. Jones, R.; Randle, V. Sensitisation behaviour of grain boundary engineered austenitic stainless steel. *Mater. Sci. Eng. A* **2010**, *527*, 4275–4280. [CrossRef]
21. Tsai, S.P.; Makineni, S.K.; Gault, B.; Kawano-Miyata, K.; Taniyama, A.; Zaefferer, S. Precipitation formation on $\sum 5$ and $\sum 7$ grain boundaries in 316L stainless steel and their roles on intergranular corrosion. *Acta Mater.* **2021**, *210*, 116822. [CrossRef]

22. Losiewica, B.; Smolka, M.P.A.; Szklarska, M.; Osak, P.; Budniok, A. Localized electrochemical impedance spectroscopy for studying the corrosion processes in a nanoscale. *Solid State Phenom.* **2015**, *228*, 383–393. [CrossRef]

23. Huang, V.M.W.; Wu, S.L.; Orazem, M.E.; Pebere, N.; Tribollet, B.; Vivier, V. Local electrochemical impedance spectroscopy: A review and some recent developments. *Electrochim. Acta* **2011**, *56*, 8048–8057. [CrossRef]

24. Wang, C.M.; Yu, J.X.; Yu, Y.; Zhao, Y.; Zhang, Y.; Han, X.X. Comparison of the corrosion and passivity behavior between CrMnFeCoNi and CrFeCoNi coatings prepared by argon arc cladding. *J. Mater. Res. Technol.* **2020**, *9*, 8482–8496. [CrossRef]

25. Wang, C.M.; Yu, Y.; Yu, J.X.; Zhang, Y.; Zhao, Y.; Yuan, Q.W. Microstructure evolution and corrosion behavior of dissimilar 304/430 stainless steel welded joints. *J. Manuf. Process.* **2020**, *50*, 183–191. [CrossRef]

26. Hasannaeimi, V.; Mukherjee, S. Galvanic corrosion in a eutectic high entropy alloy. *J. Electroanal. Chem.* **2019**, *848*, 113331. [CrossRef]

27. Poursaee, A. Determining the appropriate scan rate to perform cyclic polarization test on the steel bars in concrete. *Electrochim. Acta* **2010**, *55*, 1200–1206. [CrossRef]

28. Chen, Z.Y.; Chen, S.S.; Dou, Y.P.; Han, S.K.; Wang, L.W.; Man, C.; Wang, X.; Chen, S.G.; Cheng, Y.F.; Li, X.G. Passivation behavior and surface chemistry of 2507 super duplex stainless steel in artificial seawater: Influence of dissolved oxygen and pH. *Corros. Sci.* **2019**, *150*, 218–234.

29. Wang, C.M.; Yu, Y.; Shao, M.H.; Zhang, H. Effect of Temperature on Corrosion Behavior of Laser-remelted CrFeCoNi Coating. *Metals* **2022**, *12*, 970. [CrossRef]

30. Escriva-Cerdan, C.; Blasco-Tamarit, E.; Garcia-Garcia, D.M.; Garcia-Anton, J.; Akid, R.; Walton, J. Effect of temperature on passive film formation of UNS N08031 Cr-Ni alloy in phosphoric acid contaminated with different aggressive anions. *Electrochim. Acta* **2013**, *111*, 552–561. [CrossRef]

31. Wang, C.M.; Yu, Y.; Zhang, H.; Ma, L.X.; Wang, F.F.; Song, B.Y. Microstructure and corrosion properties of laser remelted CrFeCoNi and CrMnFeCoNi high entropy alloys coatings. *J. Mater. Res. Technol.* **2021**, *15*, 5187–5196. [CrossRef]

32. Losiewicz, B.; Kubiszta, J. Effect of hydrogen electrosorption on corrosion resistance of Pd80Rh20 alloy in sulfuric acid: EIS and LEIS study. *Int. J. Hydrog. Energy* **2018**, *43*, 20004–20010. [CrossRef]

33. Yuan, Y.; Jiang, Y.; Zhou, J.; Liu, G.; Ren, X. Influence of the grain boundary character distribution and random high angle grain boundaries networks on intergranular corrosion in high purity copper. *Mater. Lett.* **2019**, *253*, 424–426. [CrossRef]

34. Katnagallu, S.S.; Mandal, S.; Nagaraja, A.C.; de Boer, B.; Vadlamani, S.S. Role of carbide precipitates and process parameters on achieving grain boundary engineered microstructure in a Ni-based superalloy. *Metall. Mater. Trans. A. Phys. Metall. Mater. Sci.* **2015**, *46*, 4740–4754. [CrossRef]

35. Lv, J.; Wang, Z.; Liang, T.; Suzuki, K.; Hideo, M. Effect of tungsten on microstructures of annealed electrodeposited Ni-W alloy and its corrosion resistance. *Surf. Coat. Technol.* **2018**, *337*, 516–524.